

# Exploiting Intrinsic Triangular Geometry in Relativistic ${}^3\text{He}+\text{Au}$ Collisions to Disentangle Medium Properties

J. L. Nagle, A. Adare, S. Beckman, T. Koblesky, J. Orjuela Koop, D. McGlinchey, P. Romatschke<sup>1</sup> and J. Carlson, J. E. Lynn, M. McCumber<sup>2</sup>

<sup>1</sup>*University of Colorado at Boulder\**

<sup>2</sup>*Los Alamos National Laboratory*

(Dated: June 30, 2014)

Recent results in d+Au and p+Pb collisions at RHIC and the LHC provide evidence for collective expansion and flow of the created medium. We propose a control set of experiments to directly compare particle emission patterns from p+Au, d+Au, and  ${}^3\text{He}+\text{Au}$  or t+Au collisions at the same  $\sqrt{s_{NN}}$ . Using Monte Carlo Glauber we find that a  ${}^3\text{He}$  or triton projectile, with a realistic wavefunction description, induces a significant intrinsic triangular shape to the initial medium. If the system lives long enough, this survives into a significant third order flow moment  $v_3$  even with viscous damping. By comparing systems with one, two, and three initial hot spots, one could disentangle the effects from the initial spatial distribution of the deposited energy and viscous damping. These are key tools to answering the question of how small a droplet of matter is necessary to form a quark-gluon plasma described by nearly inviscid hydrodynamics.

Nearly inviscid hydrodynamic expansion of a quark-gluon plasma followed by hadronization has become the standard model for relativistic collisions of heavy nuclei at the Relativistic Heavy Ion Collider (RHIC) and the Large Hadron Collider (LHC) [1, 2]. Fluctuations in the nucleon positions within the incident nuclei result in an inhomogeneous distribution of initially deposited energy, and the influence of these spatial anisotropies survives into final state hadron momentum distributions [3]. Measurements of such flow moments,  $v_2$  for elliptic flow and  $v_3$  for triangular flow for example, probe both the initial anisotropies and the viscous damping effect through the time evolution of the medium. Striking agreement between experimental data for higher order flow moments and viscous hydrodynamic calculations with lumpy initial conditions confirm values of the shear viscosity to entropy density  $\eta/s = 1 - 2/4\pi$  [4, 5]. Similar values for  $\eta/s$  are also found in ultracold quantum gases and black holes, suggesting a much deeper connection of these strongly coupled systems [6].

Recent experimental results from central d+Au and p+Pb collisions at RHIC and the LHC, respectively, reveal remarkably similar “flow” patterns [7–10], contrary to expectations of forming no quark-gluon plasma from these small system collisions. Qualitative agreement with the  $v_2$  and  $v_3$  results is obtained with hydrodynamics [11–13], though alternative explanations involving glasma diagrams [14] and other dynamics have also been proposed. The difference in both projectile (deuteron versus proton) and center-of-mass energy ( $\sqrt{s_{NN}} = 200$  GeV versus  $\sqrt{s_{NN}} = 5.02$  TeV) between the RHIC and LHC results provides an excellent lever arm for discriminating between underlying physics explanations, though ambiguities remain.

In this paper, we propose a set of control experiments

that involve collisions of p+Au, d+Au, and  ${}^3\text{He}+\text{Au}$  or t+Au at the same  $\sqrt{s_{NN}}$ . Such a set of experiments are available to run at RHIC with modest run lengths. We utilize detailed calculations of the  ${}^3\text{He}$  and triton wavefunction for the initial distribution of nucleons within the nuclei. We then couple these distributions with Monte Carlo Glauber simulations to determine event-by-event distributions of the deposited energy. Individual events are then run through a modified version of the relativistic viscous hydrodynamic transport code [15], followed by a hadronization prescription and a hadron scattering transport code [16]. Final distributions of  $v_2$  and  $v_3$  flow coefficients as a function of transverse momentum are calculated and compared between the colliding systems and with different input parameters, including  $\eta/s$ .

As input to the Monte Carlo Glauber calculation [17], we require a realistic distribution of the nucleons within the nuclei of interest. For the Au nucleus, the nucleons are distributed following a standard Woods-Saxon distribution with radius and skin thickness parameters 6.42 fm and 0.44 fm [18]. A hard-core repulsive potential is implemented as an exclusion radius of 0.4 fm between nucleons. For the d+Au collision case, the deuteron is modeled via the Hulthen wavefunction (cf. Ref. [19]). In the case of  ${}^3\text{He}$  and triton projectiles, the three-body dynamics are important to capture as we need to model the distribution of the three hot spots created in collisions with Au nuclei. The  ${}^3\text{He}$  and triton samples come from Green’s function Monte Carlo calculations using the AV18 + UIX model interaction [20]. These calculations correctly reproduce the measured charge radii and form factors of these nuclei. The relative distribution of proton pairs in  ${}^3\text{He}$  also reproduces measurements of inclusive longitudinal electron scattering. In practice, we use a database of 10,000  ${}^3\text{He}$  configurations which correctly sample the position of the three nucleons, including correlations.

We model collisions at  $\sqrt{s_{NN}} = 200$  GeV with a nucleon-nucleon inelastic cross section of 42 mb and col-

\* jamie.nagle@colorado.edu

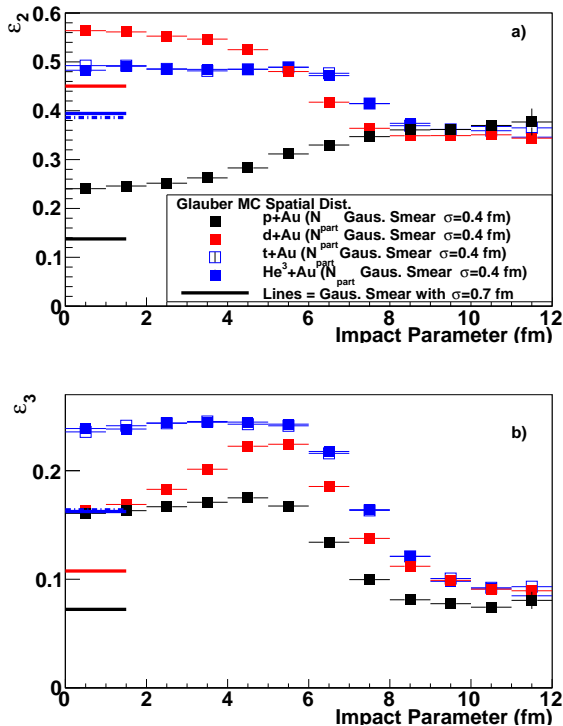


FIG. 1. (Color online) Monte Carlo Glauber results for the spatial anisotropies  $\varepsilon_2$  (panel a) and  $\varepsilon_3$  (panel b) in p+Au, d+Au,  $^3\text{He}$ +Au, and t+Au collisions at  $\sqrt{s_{NN}} = 200$  GeV as a function of impact parameter. The points are calculated with a Gaussian smearing with  $\sigma = 0.4$  fm for the energy distribution from each participating nucleon. The lines are the results for central events with a larger Gaussian smearing with  $\sigma = 0.7$  fm.

lisions at  $\sqrt{s_{NN}} = 5.02$  TeV with a nucleon-nucleon inelastic cross section of 70 mb. For each individual event, to map the positions of the participating nucleons (those with at least one inelastic collision in the event) to a distribution of energy deposited in the transverse plane, we assume that each participant contributes an equal energy with a distribution that is Gaussian around its center point with  $\sigma = 0.4$  fm, to match the RMS radius of the nucleon. There is an overall scale factor to convert these distributions to energy density, and this is determined by requiring our model to give multiplicities consistent with data in 0-5% d+Au collisions at  $\sqrt{s_{NN}} = 200$  GeV and 0-5% p+Pb collisions at  $\sqrt{s_{NN}} = 5.02$  TeV [21], respectively. For fixed  $\sqrt{s_{NN}}$ , the same factor is used for our  $^3\text{He}$ +Au, d+Au and p+Au simulations because these systems are comparable in size and we have checked that viscous heating only changes the multiplicity by less than 11 percent for  $\eta/s < 2/4\pi$ .

We have generated a million collision geometries for each case, p+Au, d+Au,  $^3\text{He}$ +Au, and t+Au, and calculated the spatial anisotropy of the initial energy distri-

bution using the following equation [3]:

$$\varepsilon_n = \frac{\sqrt{\langle r^2 \cos(n\phi_{part}) \rangle^2 + \langle r^2 \sin(n\phi_{part}) \rangle^2}}{\langle r^2 \rangle} \quad (1)$$

where  $n$  is the  $n$ th moment of the spatial anisotropy calculated relative to the mean position. These distributions are calculated with respect to the axis associated with the  $n$ th moment as defined by:

$$\psi_n = \frac{\arctan(\langle r^2 \sin(n\phi_{part}) \rangle, \langle r^2 \cos(n\phi_{part}) \rangle) + \pi}{n}. \quad (2)$$

Figure 1 shows the  $\varepsilon_2$  (elliptical) and  $\varepsilon_3$  (triangular) event-averaged values as a function of impact parameter. For central events, small impact parameter, the  $\varepsilon_2$  values are significantly larger for d+Au as compared with p+Au since the deuteron typically creates two hot spots in the interaction creating a dumbbell shaped energy distribution. The initial triangularity  $\varepsilon_3$  is largest in the  $^3\text{He}$ +Au and t+Au system. It is notable that the p+Au and d+Au central collisions induce the same  $\varepsilon_3$  since they result only from fluctuations in contrast to the intrinsic triangularity in the  $^3\text{He}$ +Au and t+Au cases. In all cases the differences between t+Au and  $^3\text{He}$ +Au are negligible and we will only refer to  $^3\text{He}$ +Au for the remainder of the paper. The lines indicate the change in the spatial anisotropies if the Gaussian smearing for each participant is increased to  $\sigma = 0.7$  fm. This has the largest impact on the p+Au case as expected since it has the smallest initial spatial scale.

We then run individual event initial conditions starting at a time  $\tau = 0.5$  fm/c through the well-tested boost-invariant relativistic viscous hydrodynamic evolution vh2 [15], modified by smearing the local energy density if it drops below one percent of the maximum value encountered at any particular instant in time. This smearing effectively avoids instabilities generated by the strong gradients present when simulating small non-homogeneous systems, while at the same time affecting bulk observables only on the per-mille level.

The results from an example  $^3\text{He}$ +Au event are shown in Figure 2. The first panel shows the temperature profile, converted from energy density using a realistic QCD equation of state [15], as generated from the above described Monte Carlo Glauber. This event has all three nucleons from the  $^3\text{He}$  nucleus striking the Au nucleus, thereby creating three hot spots. In this event, the triangular initial spatial distribution transforms into an inverted triangular distribution with maximal fluid velocity fields along the long axes of the final triangular shape.

We have run thousands of individual events for p+Au, d+Au, and  $^3\text{He}$ +Au with different values for the shear viscosity and the initial spatial distribution smearing. The final freeze-out hyper-surface of each event is then translated into a distribution of hadrons via the Cooper-Frye freeze-out prescription [22]. In Figure 3, we compare the flow coefficients from the different systems and

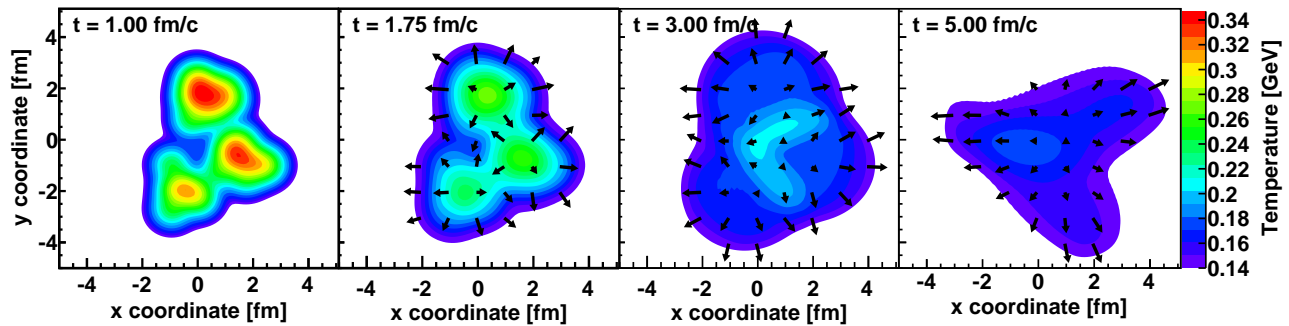


FIG. 2. (Color online) An example time evolution of a  ${}^3\text{He}+\text{Au}$  event from the initial state to final state. The color scale indicates the local temperature and the arrows are proportional to the velocity of the fluid cell from which the arrow originates.

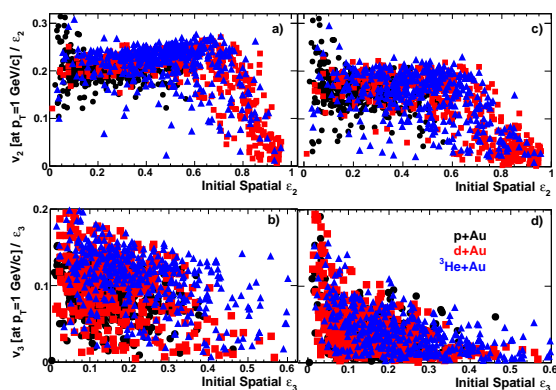


FIG. 3. (Color online)  $v_n/\varepsilon_n$  versus  $\varepsilon_n$  with the flow coefficient for pions evaluated at  $p_T = 1.0$  GeV/c from p+Au, d+Au, and  ${}^3\text{He}+\text{Au}$  central ( $b < 2$  fm) events. The results are with input parameters  $\eta/s = 1/4\pi$  and initial Gaussian smearing  $\sigma = 0.4$  fm and freeze-out temperatures of  $T_F = 150$  MeV (left) and  $T_F = 170$  MeV (right), respectively.

the scaling between initial spatial  $\varepsilon_n$  moments and final state momentum  $v_n$  values. Figure 3 shows the pion  $v_n$  at  $p_T = 1.0$  GeV/c divided by  $\varepsilon_n$  as a function of  $\varepsilon_n$  for each individual p+Au, d+Au, and  ${}^3\text{He}+\text{Au}$  event, for different freezeout temperatures  $T_F$  controlling the lifetime of the system in the plasma phase. The upper panels for  $n = 2$  shows a reasonably common scaling of  $v_2/\varepsilon_2$  for all three systems with the d+Au and  ${}^3\text{He}+\text{Au}$  simply extending to larger eccentricities with only a modest dependence on  $T_F$ . There are a small set of events with very large  $\varepsilon_2$ , but then rather small final  $v_2$ . Examination of these events reveals them to be d+Au events where the two hot spots are so far apart that the hydrodynamic fluids never connect during the time evolution, and thus there is almost no elliptic flow. There are a few  ${}^3\text{He}+\text{Au}$  in this category where two nucleons are very close and the third is quite far away, again having the same effect.

The lower panels for the  $n = 3$  case have lower values for  $v_3/\varepsilon_3$  compared to  $v_2/\varepsilon_2$  as expected from larger vis-

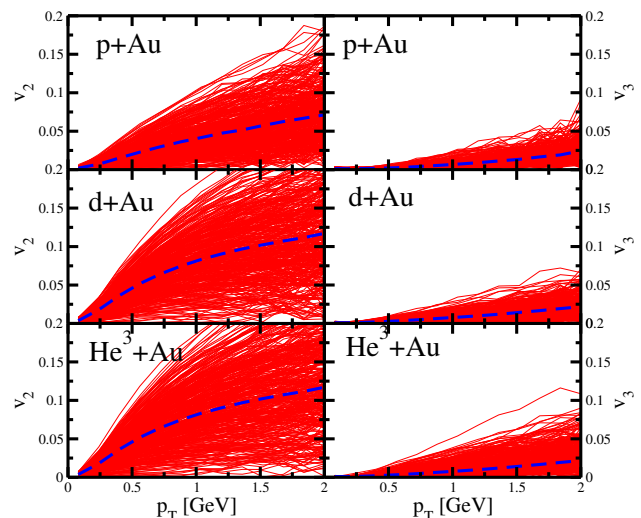


FIG. 4. (Color online) Pion momentum anisotropies  $v_2$  and  $v_3$  as a function of transverse momentum from individual p+Au, d+Au, and  ${}^3\text{He}+\text{Au}$  central ( $b < 2$  fm) events (full lines) Dashed lines are the event-averaged values.

cous damping of higher moments. There is significantly more spread of the individual events, though an overall scaling is still observed. Even more dramatic is the dependence of  $v_3/\varepsilon_3$  on  $T_F$ . Increasing  $T_F$  from 150 MeV to 170 MeV considerably shortens the hydrodynamic evolution time and results in a strong reduction of  $v_3/\varepsilon_3$  for all systems.

To reduce the dependence on  $T_F$ , we have chosen to perform a standard Cooper-Frye freezeout at  $T = 170$  MeV, followed by a hadronic cascade including resonance feed-down corrections [16]. Figure 4 shows the results for the pion momentum anisotropies  $v_2$  and  $v_3$  from 400 p+Au, 400 d+Au, and 400  ${}^3\text{He}+\text{Au}$  central ( $b < 2$  fm) events run with  $\eta/s = 1/4\pi$  and initial Gaussian smearing  $\sigma = 0.4$  fm and 10,000 cascade events for each of these hydrodynamics runs. There are substantial event-to-event differences, and the dashed lines indicate the

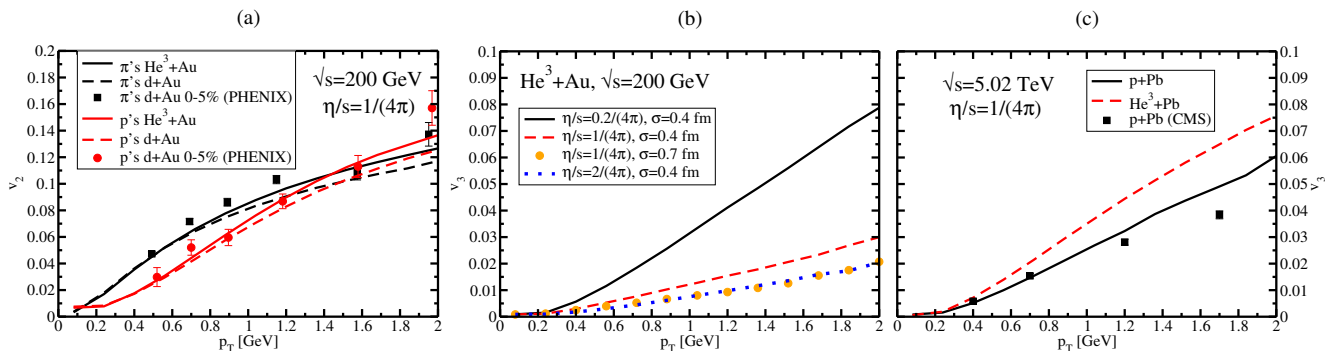


FIG. 5. (Color online) (a) pion and proton  $v_2$  versus  $p_T$  for d+Au and  $^3\text{He}+\text{Au}$  central ( $b < 2$  fm) events at RHIC energies using hydrodynamics for  $\eta/s = 1/(4\pi)$  in comparison to data for 0-5% central d+Au data from PHENIX [23]. (b) pion  $v_3$  versus  $p_T$  for  $^3\text{He}+\text{Au}$  central ( $b < 2$  fm) events at RHIC energies using viscous hydrodynamics for  $\eta/s = 0.2, 1, 2$  over  $4\pi$  as well as result of different smearing parameter  $\sigma$ . (c) pion  $v_3$  versus  $p_T$  for p+Pb and  $^3\text{He}+\text{Au}$  central ( $b < 2$  fm) events at LHC energies using viscous hydrodynamics for  $\eta/s = 1/(4\pi)$  in comparison to data for 0.5-2.5% central p+Pb data from CMS [24].

event averaged values. The d+Au event averaged  $v_2$  results are in agreement with the published experimental values [7] (cf. Figure 5(a)). The  $v_2$  values are larger in d+Au and  $^3\text{He}+\text{Au}$  compared with p+Au, and the  $v_3$  values are largest for  $^3\text{He}+\text{Au}$  as one might expect from the initial spatial anisotropies. For example,  $^3\text{He}+\text{Au}$   $v_3$  at  $p_T=1$  GeV exceeds that from d+Au and p+Au by at least 50 percent. However, we find that at energies of  $\sqrt{s_{NN}}=200$  GeV, the system stays within the plasma phase only for 2-3 fm/c. While the effect on this short system lifetime on elliptic flow  $v_2$  is seemingly rather minor, we find that there is not sufficient time to convert the initial triangularity into flow, resulting in a small overall magnitude of the triangular flow  $v_3$ .

Next we calculate the pion  $v_3$  as a function of transverse momentum with viscosity  $\eta/s = 0.2/4\pi$ ,  $\eta/s = 1/4\pi$  and  $\eta/s = 2/4\pi$ . These results are shown for  $^3\text{He}+\text{Au}$  in Figure 5(b), where the increases in viscosity have a dramatic effect in decreasing the  $v_3$  flow coefficients. It has been previously observed that an ambiguity exists between a more diffuse initial energy density (thereby reducing the  $\varepsilon_n$  values) and a larger viscous damping (thereby reducing the translation of  $\varepsilon_n$  into  $v_n$ ) [25]. This issue is significant for the smallest colliding systems, as well as ambiguities from sub-nucleonic fluctuations in calculating the initial energy density distribution [13]. For d+Au collisions, these differences are highlighted in the  $\varepsilon_n$  values tabulated with different initial geometry smearing assumptions in Table I of Ref. [19]. It is notable that the initial condition for starting hydrodynamics at time  $\tau = 0.5$  fm/c depends not only on the initial energy deposition itself, but also any pre-equilibrium dynamics during that first half fm/c.

One may posit that the geometric distribution from each participating nucleon or between participant pairs should be the same in p+Au, d+Au and  $^3\text{He}+\text{Au}$  at the same  $\sqrt{s_{NN}}$ . We thus repeat the above calculation with viscous hydrodynamics  $\eta/s = 1/4\pi$  and doubling the Gaussian smearing to  $\sigma = 0.7$  fm. The change for

central events, again defined as impact parameter  $b < 2$  fm, on the initial  $\varepsilon_2$  and  $\varepsilon_3$  mean values is shown in Figure 1. The results of this calculation on the pion momentum anisotropies are shown as the orange points in Figure 5(b). In the case of  $^3\text{He}+\text{Au}$ , comparing  $\eta/s = 1/(4\pi)$ ,  $\sigma = 0.7$  fm and  $\eta/s = 2/(4\pi)$ ,  $\sigma = 0.4$  fm, we find that there is almost complete ambiguity in the case of pion  $v_2$  and  $v_3$ , but there are strong differences for p+Au and d+Au (e.g.  $v_2$  at  $p_T=2$  GeV changes by 60 percent for p+Au). Thus, the simultaneous measurement of the flow coefficients in all three colliding systems not only provides key tests of the different explanations of these phenomena, but also a powerful methodology for discriminating different contributions to the final experimental observed anisotropies. Finally, we point out that increasing  $\sqrt{s_{NN}}$  would result in a longer system lifetime and hence a more pronounced build-up of  $v_3$ . For the case of LHC energies, we find our  $v_3$  results for p+Pb in agreement with published results by CMS and would predict a distinctively higher  $v_3$  for  $^3\text{He}+\text{Pb}$  collisions at  $\sqrt{s_{NN}}=5.02$  TeV (cf. Figure 5(c)).

In summary, we propose a novel set of measurements to control the geometry in small colliding systems by utilizing p+Au, d+Au and  $^3\text{He}+\text{Au}$  collisions. In particular, the  $^3\text{He}+\text{Au}$  geometry provides an intrinsic triangularity. The combination of measurements of different order flow moments in the different geometries will provide stringent discrimination between effects from the initial state energy deposition and pre-equilibrium dynamics and the longer time scale viscous damping during the hydrodynamic phase.

## ACKNOWLEDGMENTS

We gratefully acknowledge useful discussions with Shengli Huang, Matt Luzum and Gunther Roland. We acknowledge funding from the Division of Nuclear Physics of the U.S. Department of Energy under Grant

No. DE-FG02-00ER41152. PR acknowledges support from DOE award No. de-sc0008027 and Sloan Award No. BR2012-038. MPM acknowledges support from the Los Alamos National Laboratory LDRD project 20120775PRD4. The work of J.L., and J.C. is supported

by the U.S. Department of Energy, Office of Nuclear Physics, and by the NUCLEI SciDAC program. This research used also resources of the National Energy Research Scientific Computing Center (NERSC), which is supported by the Office of Science of the U.S. Department of Energy under Contract No. DE-AC02-05CH11231.

- 
- [1] P. Romatschke, *Int.J.Mod.Phys.* **E19**, 1 (2010), 0902.3663.
  - [2] U. W. Heinz, *J.Phys.Conf.Ser.* **455**, 012044 (2013), 1304.3634.
  - [3] B. Alver and G. Roland, *Phys.Rev.* **C81**, 054905 (2010), 1003.0194.
  - [4] B. Schenke, S. Jeon, and C. Gale, *Phys.Rev.Lett.* **106**, 042301 (2011), 1009.3244.
  - [5] B. Schenke, S. Jeon, and C. Gale, *Phys.Rev.* **C85**, 024901 (2012), 1109.6289.
  - [6] T. Schfer and D. Teaney, *Rept.Prog.Phys.* **72**, 126001 (2009), 0904.3107.
  - [7] A. Adare et al. (PHENIX Collaboration), *Phys.Rev.Lett.* (2013), 1303.1794.
  - [8] S. Chatrchyan et al. (CMS Collaboration), *Phys.Lett.* **B718**, 795 (2013), 1210.5482.
  - [9] B. Abelev et al. (ALICE Collaboration), *Phys.Lett.* **B719**, 29 (2013), 1212.2001.
  - [10] G. Aad et al. (ATLAS Collaboration), *Phys.Rev.Lett.* **110**, 182302 (2013), 1212.5198.
  - [11] P. Bozek, *Phys.Rev.* **C85**, 014911 (2012), 1112.0915.
  - [12] G.-Y. Qin and B. Mller (2013), 1306.3439.
  - [13] A. Bzdak, B. Schenke, P. Tribedy, and R. Venugopalan, *Phys.Rev.* **C87**, 064906 (2013), 1304.3403.
  - [14] K. Dusling and R. Venugopalan, *Phys.Rev.Lett.* **108**, 262001 (2012), 1201.2658.
  - [15] M. Luzum and P. Romatschke, *Phys.Rev.* **C78**, 034915 (2008), 0804.4015.
  - [16] J. Novak, K. Novak, S. Pratt, C. Coleman-Smith, and R. Wolpert (2013), 1303.5769.
  - [17] M. L. Miller, K. Reygers, S. J. Sanders, and P. Steinberg, *Ann.Rev.Nucl.Part.Sci.* **57**, 205 (2007), nucl-ex/0701025.
  - [18] T. Hirano and Y. Nara, *Phys.Rev.* **C79**, 064904 (2009), 0904.4080.
  - [19] A. Adare et al. (PHENIX Collaboration) (2013), 1310.4793.
  - [20] J. Carlson and R. Schiavilla, *Rev.Mod.Phys.* **70**, 743 (1998).
  - [21] B. B. Abelev et al. (ALICE Collaboration), *Phys.Lett.* **B726**, 164 (2013), 1307.3237.
  - [22] F. Cooper and G. Frye, *Phys.Rev.* **D10**, 186 (1974).
  - [23] A. Adare et al. (PHENIX Collaboration) (2014), 1404.7461.
  - [24] S. Chatrchyan et al. (CMS Collaboration), *Phys.Lett.* **B724**, 213 (2013), 1305.0609.
  - [25] P. Sorensen, B. Bolliet, A. Mocsy, Y. Pandit, and N. Pruthi, *Phys.Lett.* **B705**, 71 (2011), 1102.1403.